Constitutive Behavior of Tantalum and Tantalum-Tungsten Alloys

SHUH RONG CHEN and GEORGE T. GRAY III

The effects of strain rate, temperature, and tungsten alloying on the yield stress and the strain-hardening behavior of tantalum were investigated. The yield and flow stresses of unalloyed Ta and tantalum-tungsten alloys were found to exhibit very high rate sensitivities, while the hardening rates in Ta and Ta-W alloys were found to be insensitive to strain rate and temperature at lower temperatures or at higher strain rates. This behavior is consistent with the observation that overcoming the intrinsic Peierls stress is shown to be the rate-controlling mechanism in these materials at low temperatures. The dependence of yield stress on temperature and strain rate was found to decrease, while the strain-hardening rate increased with tungsten alloying content. The mechanical threshold stress (MTS) model was adopted to model the stress-strain behavior of unalloyed Ta and the Ta-W alloys. Parameters for the constitutive relations for Ta and the Ta-W alloys were derived for the MTS model, the Johnson–Cook (JC), and the Zerilli–Armstrong (ZA) models. The results of this study substantiate the applicability of these models for describing the high strain-rate deformation of Ta and Ta-W alloys. The JC and ZA models, however, due to their use of a power strain-hardening law, were found to yield constitutive relations for Ta and Ta-W alloys that are strongly dependent on the range of strains for which the models were optimized.

I. INTRODUCTION

THE microstructure/property relationships of tantalum and tantalum-based alloys continue to attract scientific and engineering interest due to their high density, melting point, excellent formability, good heat conductivity, good fracture toughness (even at low temperatures), corrosion resistance, and weldability.[1] Since 1950, numerous studies have probed the microstructure-chemistry/property response of a large number of tantalum and tantalum-based alloys, both in single-crystal and polycrystalline form.[1–5] Tantalum, like all bcc metals, exhibits deformation behavior that is markedly influenced by impurities, alloying additions, crystallographic texture, temperature, and strain rate.[2–8] Tantalum and its alloys are increasingly being utilized in defense-related applications where their mechanical properties under high strain-rate deformation are attractive. In this article, a wide range of data on unalloyed tantalum and Ta-W alloys subjected to high strain-rate compression at various temperatures will be presented. Yield and flow stresses are shown to be sensitive to the changes in temperature and strain rate at low temperatures and/or high strain rates. A large Peierls stress in bcc materials has been proposed as the rate-controlling mechanism in this temperature and strain-rate regime.[7,9] This large intrinsic lattice resistance results in restricted movement of screw dislocations; long straight screw segments are often observed in this class of materials after deformation.[3,7,10] This suppression of cross-slip of screw dislocations results in linear glide and, therefore, a lower degree of dynamic recovery. The strain-hardening rates in this class of materials at low temperature or high strain-rate loading states are seen to be temperature insensitive.[2,7] The addition of alloying solutes to tantalum raises its yield and flow stresses through solid solution strengthening.[7] The overall work-hardening rates are increased relative to unalloyed Ta due to dislocation-solute interactions. The temperature and strain-rate dependence of the yield and flow stresses, as well as the strain-hardening rate, are changed upon solute additions in commercially pure tantalum. While a large number of studies have probed the mechanical behavior of a broad spectrum of tantalum alloys, details of the underlying deformation mechanisms remain poorly understood and, in some cases, controversial.

The availability of modern high-speed computers makes it possible to develop more sophisticated material constitutive model descriptions capable of modeling complex problems.[11,12,13] An accurate description of a materials response over a wide range of loading environments, as well as having predictive capabilities outside the measured range, is in great demand. The material properties unique to bcc metals and alloys bring many challenges for the development of physically based constitutive models. The influence of impurities and the effect of tungsten alloying on the constitutive behavior of Ta and Ta-W alloys will be presented in this article. Several currently utilized constitutive models, namely the mechanical threshold stress (MTS) model,[14] the Johnson–Cook (JC) model,[15] and the Zerilli–Armstrong (ZA) model,[16] are examples of constitutive models currently implemented in a range of finite element codes, such as EPIC,[17] MESA,[18] and DYNA,[19] were examined. The same data set is used to derive the parameters for each model enabling direct comparisons between each model.

II. EXPERIMENTAL PROCEDURE

The materials used in this investigation were commercially pure (triple electron-beam) annealed unalloyed Ta plate, Ta bar stock, Ta-2.5 wt pct W (Ta-2.5W), Ta-5 wt

SHUH RONG CHEN and GEORGE T. GRAY III, Staff Members, are with the Los Alamos National Laboratory, Los Alamos, NM 87545.

Manuscript submitted March 24, 1995.

Table I. Alloy Compositions (in Weight Parts per Million Unless Otherwise Noted)

	C	O	N	H	W	Nb	Ta
Ta-A[3]	9	44	18	<1	<150	123	bal
Ta bar	10	65	20	<5	<25	80	bal
Ta	12	<50	<10	<5	60	250	bal
Ta-2.5W	18	98	<10	<5	2.4 wt pct	330	bal
Ta-5W	15	<50	<10	<5	5.2 wt pct	65	bal
Ta-10W	11	63	<10	<5	9.6 wt pct	385	bal

pct W (Ta-5W), and Ta-10 wt pct W (Ta-10W) supplied by Cabot Corporation, Boyertown, PA, with compositions, as listed in Table I. The unalloyed Ta, Ta-2.5W, and Ta-10W materials were prepared by melting 254-mm diameter or greater ingots. The Ta-5W, in contrast, was cast in a smaller research-scale electron beam melter, triple melted similar to the other ingots. All the ingots were forged into billets, the billets were annealed and cut prior to cross rolling. The plates were straight rolled in the final finishing passes. Each material was supplied in 6.35-mm-thick plate form. The as-tested microstructures of the 6.35-mm-thick unalloyed Ta, Ta-2.5W, Ta-5W, and Ta-10W plates exhibited equiaxed grains with average grain sizes of 42, 45, 48, and 42 μm, respectively.

The mechanical responses of the tantalum materials were measured in compression using solid-cylindrical samples 6.35 mm in diameter by 6.35 mm in length, lubricated with molybdenum disulfide grease. Compression samples were machined from the plates in both the through-thickness and in-plane longitudinal orientations. An initial description of the influence of tungsten alloying on the mechanical properties and texture of Ta was published previously.[20] Quasi-static compression tests were conducted at strain rates of 10^{-3} and 10^{-1} s^{-1}, at 77 and 298 K, respectively. Dynamic tests at strain rates of 1000 to 8000 s^{-1} were conducted from 77 to 1273 K in a vacuum utilizing a Split–Hopkinson pressure bar.[21] The inherent oscillations in the dynamic stress-strain curves and the lack of stress equilibrium in the specimens at low strains make the determination of yield inaccurate at high strain rates.

The shear modulus was calculated for bcc Ta using the formula

$$\mu = \frac{(C_{11} - C_{12} + C_{44})}{3} \quad [1]$$

where C_{ij} are the elastic constants.[22] For simplicity, an empirical equation[23] was used to fit the data to incorporate the temperature dependence of μ in the form of

$$\mu = \mu_0 - \frac{D}{\exp\left(\frac{T_0}{T}\right) - 1} \quad [2]$$

where μ_0, D, and T_0 are fitting constants. The same temperature-dependent shear modulus was used for the Ta-W alloys.

III. DESCRIPTION OF MODELS

The constitutive equations used in this study have the following forms.

A. *JC Model*[15]

$$\sigma = (A + B \cdot \varepsilon_p^n)(1 + C \cdot \ln \dot{\varepsilon}^*)(1 - T^{*m}) \quad [3]$$

where $\dot{\varepsilon}^*$ is a nondimensional strain-rate value, ε_p is the plastic strain, and T^* is $(T - T_{room})/(T_{melt} - T_{room})$. The value of T is in degrees kelvin, and A, B, n, C, and m are constants for this model.

B. *ZA Model for bcc Materials*[16]

$$\sigma = C_0 + C_1 \cdot \exp(-C_3 \cdot T + C_4 \cdot T \cdot \ln \dot{\varepsilon}) + C_5 \cdot \varepsilon_p^n \quad [4]$$

where C_0, C_1, C_3, C_4, C_5, and n are constants for this model. The athermal stress term C_0 can be replaced with a Hall–Petch relation $\sigma_0 + k \cdot d^{-1/2}$, where d is the grain size, to address a grain size dependence on the yield stress.[16] In the ZA model, it is presumed that the work-hardening rate is independent of temperature and strain rate. Both of the preceding models use a power-law stress-strain relationship that exhibits continual work hardening without approaching a saturation in the flow stress at large strains.

For the JC and ZA models, computer programs were developed[24] to optimize the fitting constants to the stress-strain data over a wide range of temperatures and strain rates. A range of corresponding constants is given to calculate the stress at a certain strain followed by a comparison of this value to the experimental values. This process is repeated for every curve of interest until the best agreement to the entire set of stress-strain data is achieved. A parameter indicating the degree of fit is defined as

$$\delta = \frac{\sum_{i=1}^{k} \frac{|\sigma_{calculated}(\varepsilon_i) - \sigma_{experimental}(\varepsilon_i)|}{\sigma_{experimental}(\varepsilon_i)}}{k} \quad [5]$$

Four points representing the characteristic hardening behavior for each stress-strain curve were taken to compare the calculated stresses at the corresponding strain values. For the modeling results presented in this article, fits with deviation parameters of better than 4 pct were achieved.

C. *MTS Model*

The framework and detailed description of the MTS model are given elsewhere.[14,25,26] A summary of the MTS model is presented here to facilitate comparisons with the JC and ZA models and discussion of the results. Plastic deformation is known to be controlled by the thermally activated interactions of dislocations with obstacles. In the MTS model, the current structure of a material is represented by an internal state variable, the mechanical threshold ($\hat{\sigma}$),[27] which is defined as the flow stress at 0 K. The mechanical threshold is separated into athermal and thermal components:

$$\hat{\sigma} = \hat{\sigma}_a + \Sigma \hat{\sigma}_t \quad [6]$$

where the athermal component $\hat{\sigma}_a$ characterizes the rate-independent interactions of dislocations with long-range barriers, such as grain boundaries, dispersoids, or second phases. The thermal component $\hat{\sigma}_t$ characterizes the rate-dependent interactions of dislocations with short-range ob-

stacles (*i.e.*, forest dislocations, interstitial, solutes, Peierls barrier, *etc.*) that can be overcome with the assistance of thermal activation. The summation of the contributions from different obstacles does not need to be linear.[25] The flow stress of a constant structure at a given deformation condition can be expressed in terms of the mechanical threshold as

$$\frac{\sigma}{\mu} = \frac{\sigma_a}{\mu} + \sum \frac{\sigma_t}{\mu} = \frac{\sigma_a}{\mu} + \sum S(\dot{\varepsilon},T)\,\frac{\hat{\sigma}_t}{\mu_0} \qquad [7]$$

where the athermal component is a function of temperature only through the shear modulus, and the factor S specifies the ratio between applied stress and mechanical threshold stress. This factor is smaller than one for thermally activated controlled glide because the contribution of the thermal activation energy reduces the stress required to force a dislocation past an obstacle. In the thermally activated glide regime, the interaction kinetics for short-range obstacles are described by an Arrhenius expression of the form

$$\dot{\varepsilon} = \dot{\varepsilon}_0 \exp\left(\frac{-\Delta G}{kT}\right) \qquad [8]$$

The free energy (ΔG) is a function of stress and a phenomenological relation was chosen[27]

$$\Delta G = g_0 \mu b^3 \left[1 - \left(\frac{\sigma_t/\mu}{\hat{\sigma}_t/\mu_0}\right)^p\right]^q \qquad [9]$$

g_0 in units of μb^3 is the normalized activation energy for the dislocations to overcome the obstacles. It is also an indication of the sensitivity of overcoming this obstacle to changes in temperature and strain rate. The terms p and q are parameters with the ranges $0 < p \leq 1$ and $1 \leq q \leq 2$. They detail the glide resistance profile in the higher and lower activation energy regions, respectively.[27] Upon rearrangement, we have the following relation between applied stress (σ_t) and mechanical threshold stress ($\hat{\sigma}_t$) at a constant structure...

$$\frac{\sigma_t}{\mu} = \left[1 - \left(\frac{kT}{g_0 \mu b^3} \ln \frac{\dot{\varepsilon}_0}{\dot{\varepsilon}}\right)^{1/q}\right]^{1/p} \cdot \frac{\hat{\sigma}_t}{\mu_0} \qquad [10]$$

For single-phase materials with cubic crystal structures, the thermal component (σ_t) consists of the linear summation of a term describing the thermal portion of the yield stress ($\sigma_t = \sigma_y - \sigma_a$) and a term describing the evolution of the dislocation structure σ_ε as a function of temperature, strain rate, and strain. Eq. [7] can be written as

$$\frac{\sigma}{\mu} = \frac{\sigma_a}{\mu} + \frac{\sigma_t}{\mu} + \frac{\sigma_\varepsilon}{\mu} = \frac{\sigma_a}{\mu} + S_t(\dot{\varepsilon},T)\,\frac{\hat{\sigma}_t}{\mu_0} + S_\varepsilon(\dot{\varepsilon},T)\,\frac{\hat{\sigma}_\varepsilon}{\mu_0} \qquad [11]$$

The second term on the right-hand side of the equation describes the rate-dependent portion of the yield stress, mainly due to intrinsic barriers, such as the strong Peierls stress in bcc materials at low temperatures or at high strain rates. It is further assumed that this term does not evolve after yielding. The term $\hat{\sigma}_\varepsilon$ in Eq. [11] evolves with strain due to dislocation accumulation (work hardening) and annihilation (recovery). This structure evolution, $\theta = d\hat{\sigma}/d\varepsilon$, is written as

$$\theta = \theta_0 - \theta_r(T,\dot{\varepsilon},\hat{\sigma}) \qquad [12]$$

where θ_0 is the hardening due to dislocation accumulation and θ_r is the dynamic recovery rate. The physical understanding of the work-hardening behavior of polycrystals is still inadequate to unify this complex process and represent it entirely by physically based parameters. Follansbee and Kocks[14] have selected the following form to fit their experimental hardening data for Cu, and the same form was found to provide a robust fit to hardening behavior in Ni[26] and Ti-6Al-4V:[25]

$$\theta = \theta_0 \left\{1 - \frac{\tanh\left[\alpha \dfrac{\hat{\sigma}_\varepsilon}{\hat{\sigma}_{\varepsilon s}(\dot{\varepsilon},T)}\right]}{\tanh(\alpha)}\right\} \qquad [13]$$

where α approaching zero represents a linear variation of strain-hardening rate with stress (Voce law). The saturation threshold stress $\hat{\sigma}_{\varepsilon s}$ is a function of temperature and strain rate. Kocks[28] has proposed a description for $\hat{\sigma}_{\varepsilon s}$ that has the same form as that proposed by Haasen[29] for the beginning of dynamic recovery, which in turn, was based on calculations by Schoeck and Seeger[30] of the stress dependence of the activation energy for cross slip in fcc metals. The relation is written

$$\ln \frac{\dot{\varepsilon}}{\dot{\varepsilon}_{\varepsilon s 0}} = \frac{g_{0\varepsilon s}\,\mu b^3}{kT} \ln \frac{\hat{\sigma}_{\varepsilon s}}{\hat{\sigma}_{\varepsilon s 0}} \qquad [14]$$

where $\dot{\varepsilon}_{\varepsilon s 0}$, $g_{0\varepsilon s}$, and $\hat{\sigma}_{\varepsilon s 0}$ are constants.

IV. RESULTS AND ANALYSIS

A. *Compression Test Results*

The compressive stress-strain responses of unalloyed Ta and Ta-W alloys at 25 °C and 500 °C as a function of Ta-alloying content and strain rate are shown in Figure 1. The lower yield and flow-stress levels in the tantalum and tantalum alloys are seen to increase with increasing strain rate. As observed in many bcc materials at low temperature or at high strain rate, these materials show very high strain-rate sensitivities in their yield and flow stresses. The addition of tungsten to tantalum results in an increase in the yield stress and flow stress in Ta-W alloys in a similar way to increasing the strain rate for unalloyed tantalum. The room temperature stress-strain response of unalloyed tantalum at a strain rate of 2500 s^{-1} is very close to that exhibited by Ta-10W deformed quasi-statically at a strain rate of 10^{-3} s^{-1} at 25 °C (Figure 1). This observation is consistent with the well-established solute strengthening effects of tungsten alloying additions on Ta.[2,3,31]

The strain-rate and alloying effects of W on the flow-stress response of tantalum are quantified further in Figure 2, where the stress level at high strain rates, designated (hr), and low strain rates, designated (Lr), at two different strain values are plotted *vs* the tungsten alloying content in weight

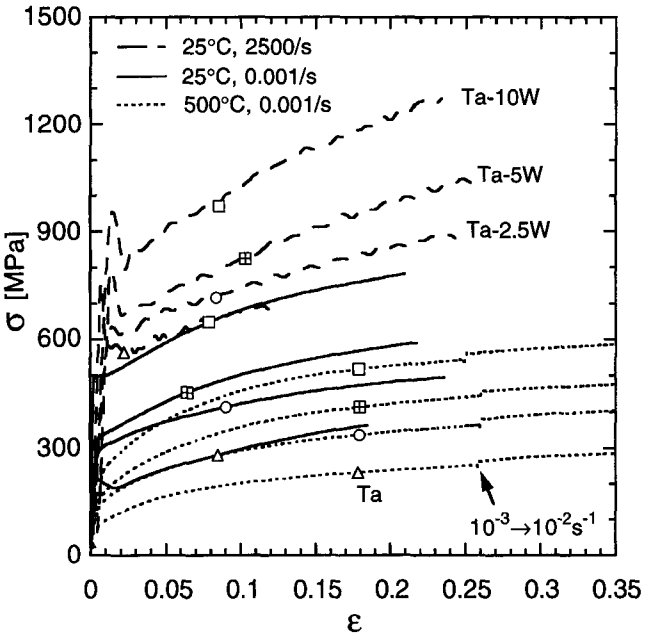

Fig. 1—Compressive stress-strain response of Ta, Ta-2.5W, Ta-5W, and Ta-10W at strain rates of 2500 and 10^{-3} s^{-1} at 25 °C and at strain rates of 10^{-3} s^{-1} at 500 °C.

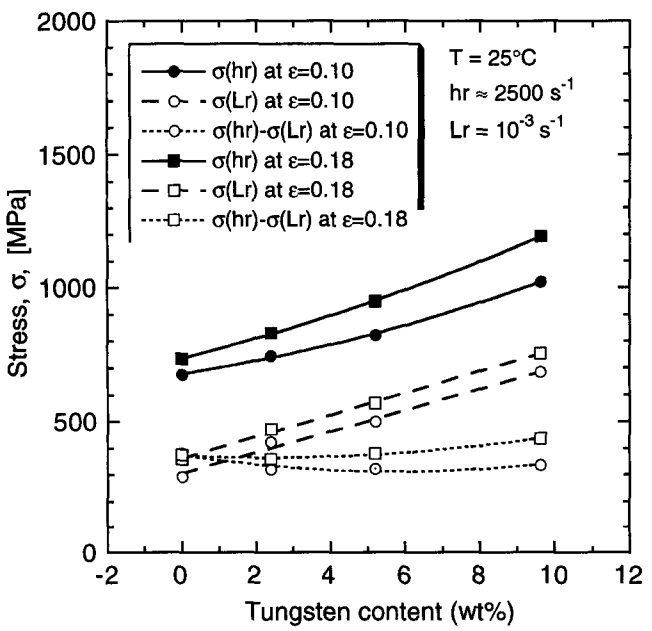

Fig. 2—Room temperature flow stresses at strains of 0.1 and 0.18 at strain rates of 2500 and 10^{-3} s^{-1} as a function of tungsten alloying content in tantalum.

percent. The flow-stress levels at low strain rate are seen to increase linearly with alloying content (dashed lines with open symbols in Figure 2). At two different strain values (0.1 and 0.18), the linearity between the flow stresses and the tungsten content is preserved with the same functional relationship suggesting that tungsten alloying does not alter the strain-hardening behavior of these materials deformed at low strain rates at room temperature. The flow stresses obtained at the same strains under dynamic loading (solid lines with solid symbols in Figure 2) increase nonlinearly with respect to the alloying content compared to that exhibited under quasi-static conditions. The difference in the

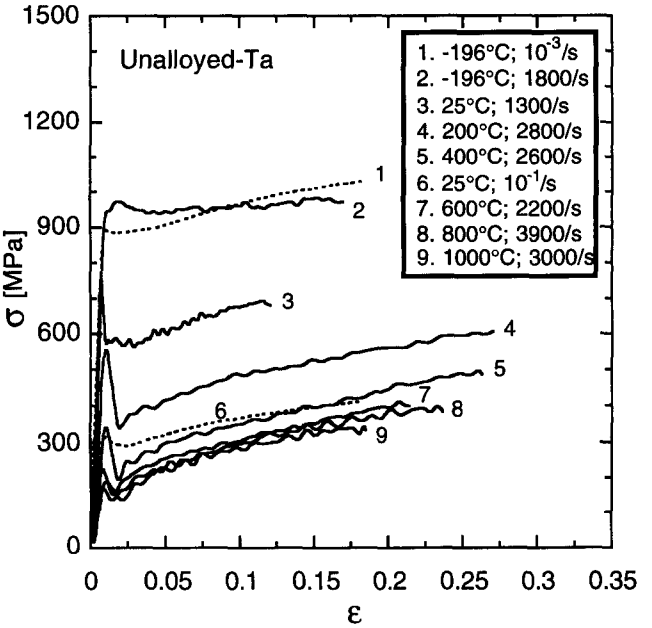

Fig. 3—Compressive stress-strain curves of the unalloyed tantalum under dynamic and quasi-static deformation at various temperatures.

stress levels at high strain rate, for strains of 0.1 and 0.18, increases with increasing alloying content. This divergence reveals the increase in strain-hardening rate commensurate with increasing tungsten content in tantalum. The flow-stress differences between high and low strain-rate compression, given in Figure 2 as the finely dotted lines, increase with increasing tungsten content, except for the unalloyed tantalum which exhibits a higher difference than from alloying with 2.5 pct tungsten. This discrepancy can be explained in terms of the high sensitivity of the flow stress in bcc materials to impurities at low temperature or high strain rate. Alloying with an ample quantity of tungsten tends to overshadow the impurity effects observed in less pure tantalum.[20] The flow-stress decrease after yielding, which was interpreted as an influence of impurities, during quasi-static deformation at 25 °C, disappears when tantalum is alloyed with 2.5 or 5 pct tungsten or when the materials are deformed at elevated temperatures, as shown in Figure 1. The flatness of the slopes of the curves describing the stress differences further indicates that the major influence of tungsten alloying on the mechanical properties of tantalum is to: (1) substantially raise the yield and flow stresses of tantalum with tungsten alloying, and (2) either weakly, as in the case of the 2.5 or 5 wt pct alloys, or moderately, as in the case of the 10 wt pct alloy, affect the strain-hardening response of tantalum.

The effect of temperature and strain rate on mechanical properties of unalloyed and alloyed tantalum was investigated through a series of compression tests at different temperatures and strain rates. The results for the unalloyed tantalum are plotted in Figure 3. Below 200 °C, this material exhibits a high temperature and strain-rate sensitivity. Increasing the test temperature by the same increment (200 °C) but over two different temperature ranges shows that the difference in stress response diminishes. The constitutive response shows less temperature sensitivity at higher temperatures, as demonstrated by the curves numbered 7, 8, and 9 *vs* curves 3, 4, and 5 in Figure 3. This behavior

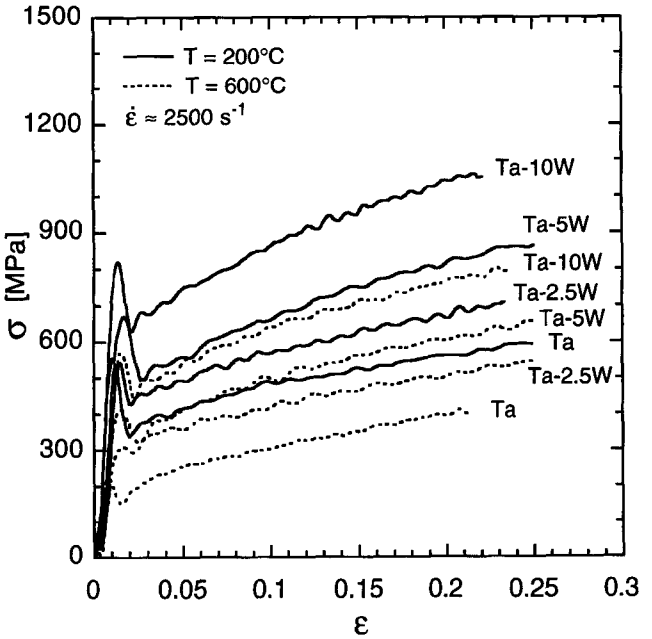

Fig. 4—Compressive stress-strain curves for Ta and Ta-W alloys deformed dynamically at 200 °C and 600 °C.

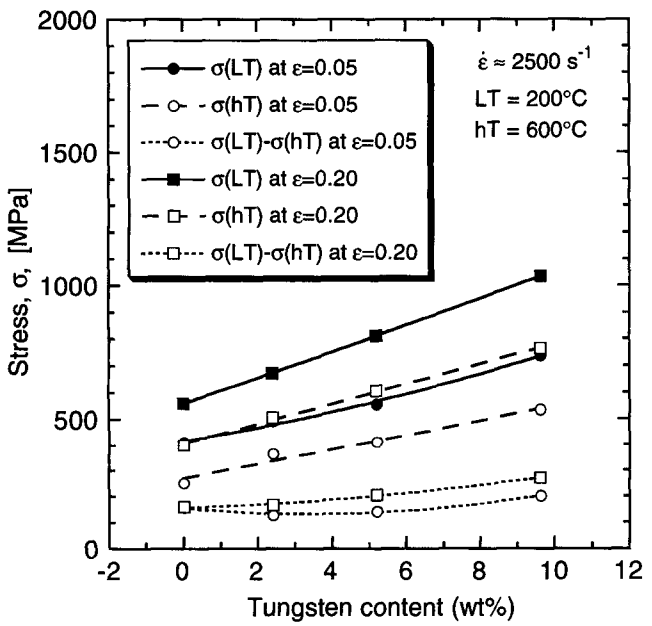

Fig. 5—Dynamic flow stresses at strains of 0.05 and 0.2 at temperatures of 200 °C and 600 °C as a function of tungsten alloying content in the Ta-W alloys studied.

is primarily due to dislocations overcoming the intrinsic short-range obstacle(s), such as strong Peierls stress. The intrinsic barrier(s) that exhibits very high temperature and strain rate sensitivities becomes transparent to dislocation motion at higher temperatures through thermal activation process. The dependence of the flow stress on temperature, therefore, dramatically decreases. However, the strain-hardening behavior is essentially unchanged, even when deformed at 1000 °C at a high rate, as compared to room temperature and high strain rate.

The effect of temperature on the stress-strain response of alloyed tantalum is illustrated in Figure 4, which is a plot consisting of unalloyed Ta, Ta-2.5W, Ta-5W, and Ta-10W deformed at a high strain rate at two different temperatures, namely, 200 °C and 600 °C. Within this range, all the materials show a relatively high sensitivity to the temperature change. The strain-hardening rate decreased when the test temperature increased for Ta-5W and Ta-10W. Less of an effect was observed for the hardening behavior of unalloyed Ta or Ta-2.5W. Figure 5 correlates the stress levels taken from Figure 4 at two different strains of 0.05 and 0.2, respectively, and plots them as a function of tungsten content. Overall, the result is similar to that, as shown in Figure 2, in which the strain rate was changed instead of the temperature. This result further supports that the deformation processes in Ta and Ta alloys can be explained in terms of thermal activation theory, which requires that temperature and strain rate are coupled in a form of $kT \cdot \log(\dot{\varepsilon}_0/\dot{\varepsilon})$, which is rearranged from Eq. [8]. Increasing (decreasing) the strain rate logarithmically has the same effect as decreasing (increasing) the temperature linearly. The stress increase observed at a low temperature, mainly due to solid solution hardening of W, remains at high temperatures. The change in strain-hardening rate varies from almost nothing for unalloyed Ta to a moderate degree for Ta-10W, as indicated by the separation of these two dotted lines in Figure 5, which represents the stress increment at strains of 0.05 and 0.2, respectively. If the strain-hardening rate remains unchanged, these two points will be coincident, as is shown for the unalloyed Ta. As deformation continues, the divergence of the stress-strain curves results from changes in the strain-hardening rate. This will be reflected in the separation of the two dotted lines and symbols, which is precisely what is seen in Figure 5.

B. *Constitutive Modeling*

1. *JC and ZA models*

The basic approach to fitting the JC and ZA models is to select a wide range of data to represent the temperature and strain-rate sensitivity, as well as the hardening behavior of a given material. A range of corresponding parameters (A, B, n, C, and m in the JC model; C_0, C_1, C_3, C_4, C_5, and n in the ZA model) varied by specified increments are then tested in a computer optimization routine developed for the personal computer to compare the calculated and experimental stress levels at certain strains for all the data. Minimum deviation of the calculated stress from the experiment is used as a guideline to judge the fitting. This process is repeated and the range of the parameters is decreased as well as the increment for each parameter. In general, to calculate a few hundred thousand sets of parameters to fit ten stress-strain curves takes about 5 minutes. Less than five adjustments to the parameter range and increment were found to give a best fit to the data. Because no single parameter is dominant or redundant, this optimization for the whole spectrum of data of interest does yield a best set of parameters without excessive prejudgement. A comparison of the results derived for tantalum, from the tantalum data of Hoge and Mukherjee,[9] by Zerilli and Armstrong[32] and by the current method was recently presented.[24] It was concluded that the current parameter optimization method is as satisfactory as or better than the method used originally.

The fit to the ZA model for unalloyed Ta is shown in Figure 6. The experimental data at strains less than 0.2 were treated as an isothermal condition for all strain rates. The

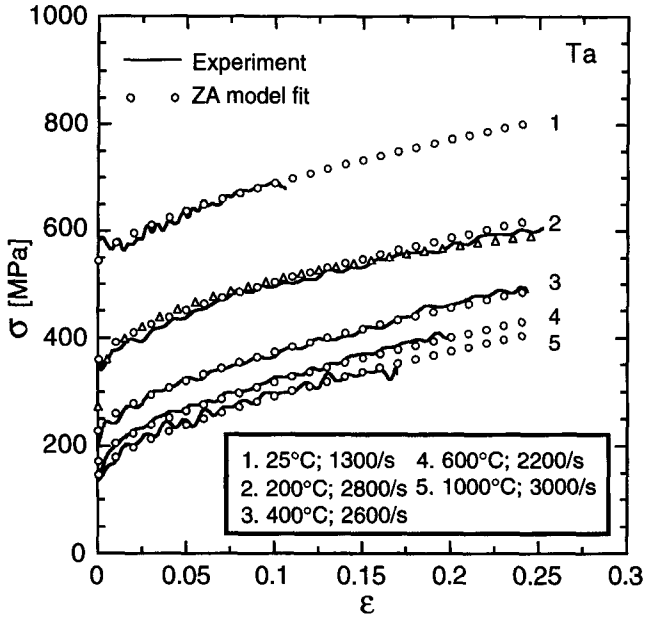

Fig. 6—The stress-strain curves of unalloyed tantalum showing the fit to the ZA model as the open circles.

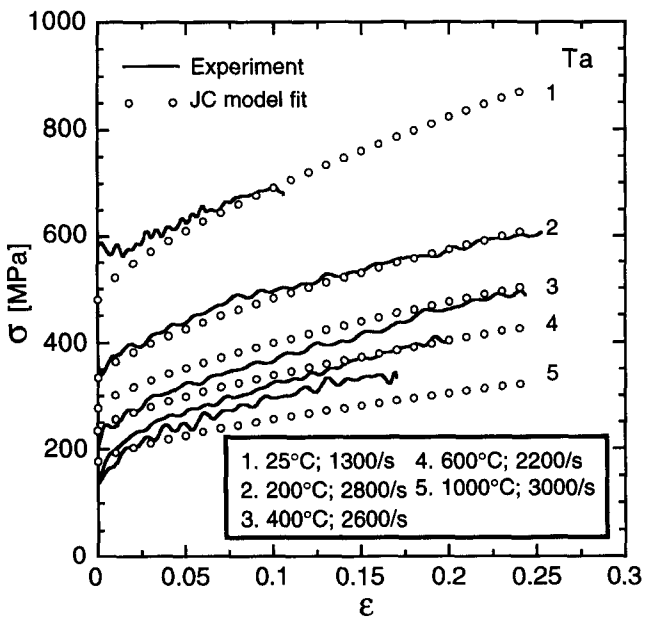

Fig. 7—The stress-strain curves of unalloyed tantalum showing the fit to the JC model as the open circles.

effect of adiabatic heating at high strains rate was neglected for low strains. In order to make an isothermal curve, a relation between temperature and stress has to be assumed that may not be accurate and, therefore, introduce uncertainties to the stress levels. A possible approach in the future will be to assume there is not much temperature change at strains less than 0.2 then fit the data set as the isothermal condition. After a better description between temperature and stress is obtained, this relation can be used to correct the original curves for adiabatic heating. Finally, the temperature-corrected curves can be refit to the model to derive the final fitting parameters. The temperature increase for tests at strain rates above 500 s^{-1} can be calculated assuming a certain percentage (Ψ) of the work of plastic deformation is converted into heat according to

$$\Delta T = \frac{\Psi}{\rho C_p} \int \sigma(\varepsilon) d\varepsilon \qquad [15]$$

where σ and ε are the true stress and strain, ρ is the density, and C_p is the heat capacity that can be written in the form of $A_0 + A_1 \cdot T + A_2/T^2$.[33] Adiabatic heating makes a large difference at higher strains under high rate deformation.

Fitting results for Ta to the ZA model are good for strain rates from 10^{-3} s^{-1} (not shown in the figure) to the rate of 5000 s^{-1}, and over the temperature range of 25 °C to 1000 °C (Figure 6). The fit to the JC model to the same data set is shown in Figure 7. The formulation of the JC model, Eq. [3], presumes that the stress-strain curves diverge upon increasing deformation after yield. However, in this study, we have shown that the strain-hardening rate is insensitive to strain rate and temperature in unalloyed Ta within the range investigated. Substantial deviations of the model predictions from the experimental data for the Ta strain-stress data at 25 °C and at 1000 °C for the JC model are seen. The fitting parameters for the unalloyed Ta and Ta-W alloys studied are listed in Table II and III for the ZA and JC models, respectively.

Table II. Fitting Parameters for ZA Model

	C_0 (MPa)	C_1 (MPa)	C_3 (K^{-1})	C_4 ($K^{-1} \cdot s^{-1}$)	C_5 (MPa)	n
Ta	140	1750	0.00975	0.000675	650	0.650
Ta bar	25	1040	0.00525	0.000300	480	0.575
Ta-2.5W	140	1300	0.00825	0.000525	650	0.400
Ta-5W	140	950	0.00650	0.000425	775	0.400
Ta-10W	140	900	0.00550	0.000325	1200	0.350
Ta*	55	1750	0.00975	0.000675	510	0.338
Ta bar*	5	1200	0.00650	0.00035	390	0.300
Ta-2.5W*	55	1300	0.00825	0.000525	735	0.325
Ta-5W*	55	950	0.00500	0.000325	780	0.375
Ta-10W*	50	950	0.0055	0.000325	1200	0.300
Ta[32]	30	1125	0.00535	0.000327	310	0.440

*Enforcing the stress-strain behavior at large strains as predicted by the MTS model.

Table III. Fitting Parameters for JC Model

	A (MPa)	B (MPa)	n	C	m	T_m (K)
Ta	340	750	0.7	0.0575	0.400	3250
Ta-2.5W	390	700	0.575	0.0400	0.500	3250
Ta-5W	400	875	0.525	0.0363	0.550	3250
Ta-10W	470	1000	0.425	0.0300	0.600	3250
Ta*	220	520	0.325	0.0550	0.475	3250
Ta-2.5W*	270	650	0.325	0.0375	0.600	3250
Ta-5W*	290	800	0.325	0.0388	0.563	3250
Ta-10W*	300	1025	0.275	0.0300	0.650	3250
Ta[24]	185	675	0.300	0.0470	0.425	3250

*Enforcing the stress-strain response at large strains as predicted by the MTS model.

2. *Mechanical threshold model*

As stated in Eq. [11], the contribution to the flow stress arising from different obstacles has to be examined to achieve a physically based modeling fit. Athermal stress depends on the temperature through the shear modulus

only, and it is a constant after being normalized by the shear modulus. Based on previous tantalum data[3,34,35] over a wide range of strain rates and temperatures, a value of 3×10^{-4} for σ_a/μ was chosen. Athermal stress has been shown to be a function of alloying concentration in Ta-W single crystals.[31] The critical resolved shear stress was ≈80 MPa at 25 °C and ≈5 MPa at 1800 °C for a pure Ta single crystal while it was ≈190 MPa at 25 °C and ≈10 MPa at 1800 °C for a Ta-3.75 at. pct W single crystal oriented for single slip. Athermal stress was even lower than the yield stress at 1800 °C. The small fraction of the athermal stress, with respect to the higher yield stress, exhibited within the temperature range for the Ta and Ta-W alloys and the constitutive models applied to them makes an accurate selection of the athermal stress actually insignificant in the analysis. This is mainly used to take grain size effect into consideration. The second term on the right-hand side of Eq. [11] represents the thermal contribution to the yield stress on top of the athermal contribution. It is further assumed that it does not evolve with strain. In well-annealed materials, the initial dislocation density is low enough so that the contribution from the strain-hardening term at very low strains can be neglected. From the plot of the yield stress (σ_y) as a function of the normalized activation energy, the corresponding parameters which describe the deviation from the mechanical threshold ($\hat{\sigma}_i$) as a function of temperature and strain rate can be determined. The governing Eqs. [10] and [11] can be rearranged as

$$\left(\frac{\sigma_y - \sigma_a}{\mu}\right)^{p_i} = \left(\frac{\hat{\sigma}_i}{\mu_0}\right)^{p_i} - \left(\frac{kT}{g_{0i}\mu b^3} \ln \frac{\dot{\varepsilon}_{0i}}{\dot{\varepsilon}}\right)^{1/q_i} \cdot \left(\frac{\hat{\sigma}_i}{\mu_0}\right)^{p_i} \quad [16]$$

where $\dot{\varepsilon}_{0i}$ is an adjustable parameter. An optimum value of $\dot{\varepsilon}_{0i}$ will bring all the data at different temperatures and strain rates into a single curve. The term g_{0i} is the normalized activation energy for the dislocations to overcome the intrinsic barrier(s) or to unpin from impurities or solutes. It is also an indication of the sensitivity of overcoming this obstacle to changes in temperature and strain rate. The terms p_i and q_i are parameters previously defined in Eq. [9].

The results of the preceding analysis, which unified several state parameters in the MTS model for the Ta and Ta-W alloys, are shown in Figure 8. Extensive study on a previous tantalum Ta-A,[3,34] with the composition listed in Table I, will be published elsewhere with an emphasis on dynamic strain aging. This material contained slightly less impurities than the unalloyed Ta. After the data was plotted according to Eq. [16], it is clear that two distinct deformation regimes are associated with this material under different testing conditions. Each has its own dominant rate-controlling mechanism. Within the low normalized activation energy region (lower temperature, higher strain rate, indicated as region 1 in Figure 8), g_{0i} is relatively small. It is 0.123 for the Ta-A and 0.133 for the unalloyed Ta in this study. This value increases to 0.178 for the Ta-2.5W, 0.210 for the Ta-5W, and 0.280 for the Ta-10W. The small values of the normalized activation energy suggest that the rate-controlling mechanism in these materials is overcoming the Peierls barrier, which has a small activation volume.[9,36] Increasing the W content in Ta decreases the rate sensitivity of the alloy. However, dislocations are more difficult to move due to solution hardening, thereby increasing the yield strength in Ta-W alloys. Nevertheless, the small change in the normalized activation energy suggests that the rate-controlling mechanism remains the Peierls barrier in both unalloyed and alloyed Ta. There is a reasonably sharp transition when the normalized activation energy is higher than a certain value, which seems to be a function of the material composition; the slope of the curve changes dramatically to yield a much higher g_{0i}. In this region (indicated by 2 in Figure 8), yield stress is not a strong function of temperature or strain rate. Dislocation pinning[37] by interstitial impurities (in the unalloyed Ta) or by solutes (in the W alloying Ta) is believed to be the rate-controlling mechanism in this regime. A limited number of data points at higher temperatures were obtained for the unalloyed Ta and Ta-W alloys and are shown in Figure 8. The long dashed line in the lower activation energy region was the best fit to the data for the Ta-5W. Extrapolating this curve to a test at 500 °C at 10^{-3} s^{-1} will predict a normalized yield stress at a value less than 0.1, which is marked as a "+" in Figure 8. This low yield stress is not reasonable because it is much lower than the one exhibited by the unalloyed Ta. An experimental data point is plotted as the solid triangle directly above the cross symbol in Figure 8. It is seen that a second regime, mainly under higher temperatures with a different rate-controlling mechanism, also exists for the Ta-W alloys. Based on the slopes of the fitted dashed lines for the Ta-5W alloy as opposed to that of the solid lines for the unalloyed Ta, it is suggested that the temperature and strain-rate sensitivity of the tantalums is significantly modified by W alloying. Alloying with W makes the change from region 1 to region 2 less apparent due to an increase in the importance of dislocation-solute interactions when the solute concentration is increased. Additional high temperature/lower strain-rate experiments are needed to accurately determine the normalized activation energy g_{0i2}, and to precisely derive the demarcation for the transition between regions 1 and 2.

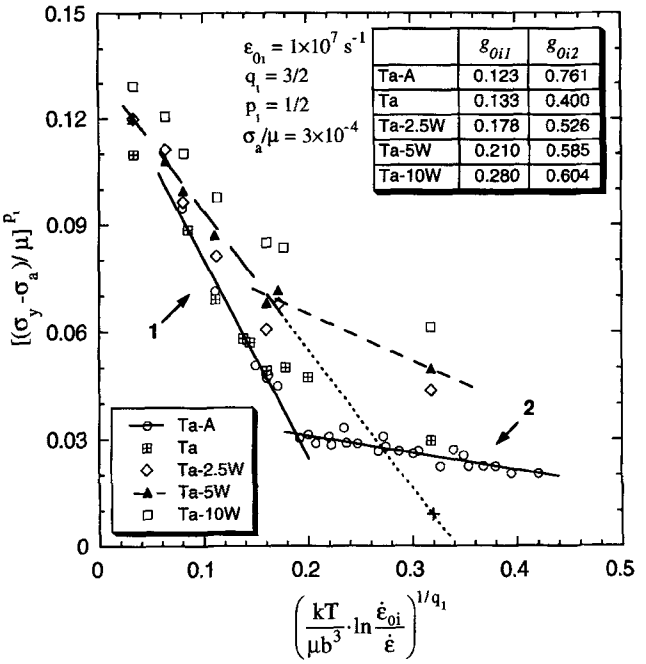

Fig. 8—Yield stresses of Ta and Ta-W alloys plotted according to Eq. [16]. The g_{0i2} of the unalloyed Ta and Ta-W alloys was calculated from a limited number of high temperature data.

The next step toward a complete constitutive relation for the MTS model is the description of strain hardening due to dislocation storage. The constants used in Eqs. [10] through [14] are next determined from the experimental data. For each $\sigma(\varepsilon)$ curve, a corresponding mechanical threshold $\hat{\sigma}_\varepsilon(\varepsilon)$ is derived according to

$$\hat{\sigma}_\varepsilon(\varepsilon) = \frac{\mu_0}{S_\varepsilon}\left(\frac{\sigma(\varepsilon)}{\mu} - \frac{\sigma_a}{\mu_0} - S_i\frac{\hat{\sigma}_i}{\mu_0}\right) \qquad [17]$$

The constants used in the S_ε factor were $\dot{\varepsilon}_{0\varepsilon} = 10^7\ s^{-1}$, $g_{0\varepsilon} = 1.6$, $p_\varepsilon = 2/3$, and $q_\varepsilon = 1$, with $g_{0\varepsilon}$ the more critical parameter, based on previous experience with Cu[14] and other materials.[25,26] The hardening curve at 0 K was fitted to Eq. [13] to obtain the saturation stress of the mechanical threshold. This saturation stress at 0 K was calculated for each test condition, and the results were plotted according to Eq. [14] to derive the remaining parameters. Final model-fitting results for the unalloyed Ta are shown in Figure 9. The constants of the MTS model for Ta and the Ta-W alloys are summarized in Table IV.

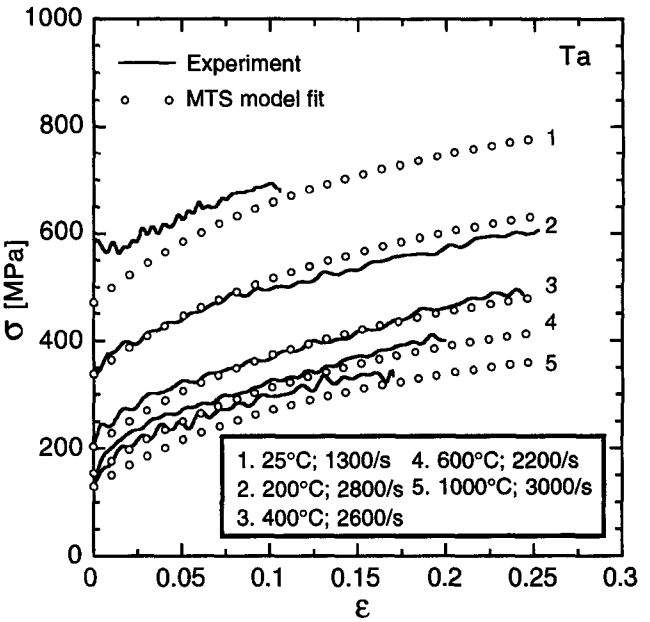

Fig. 9—The stress-strain curves of unalloyed tantalum showing the fit to the MTS model as the open circles.

V. DISCUSSION

A. *Description of Hardening Behavior in Constitutive Models*

In general, material structure evolves as a result of the imposed external stresses. The description of structure evolution is important in constitutive models. One of the most commonly used equations for many decades to describe the stress-strain curves of polycrystalline metals is due to Ludwik[38] in 1909. Stress increases according to a power function with respect to the strain in the following way

$$\sigma = \sigma_0 + K \cdot \varepsilon^n \qquad [18]$$

where σ_0, K, and n are material constants. This form of hardening behavior was adopted into the constitutive models by Johnson and Cook[15] and Zerilli and Armstrong.[16] It is generally accepted however, that at large strains most metallic materials tend to approach a finite "saturation stress"[28] or approach a constant but small hardening rate at large strains (stage IV).[39,40] Such a saturation is lacking in the form of Eq. [18]. The MTS model contrarily uses a differential form as written in Eq. [13] to fit the experimental data. The ill-defined integrated strain (from the entire previous deformation history) is thereby avoided. The parameter α determines how a material reaches saturation. With the saturation concept built in and a differential form of a hardening law in place, the data obtained under a well-controlled condition to a reasonable value of strain are sufficient to derive all the parameters needed in Eq. [13]. In the JC and ZA models, for large-strain applications, as seen for example in ballistics or metal forming, stress-strain data at large strains are, therefore, essential for deriving the constants for these models. Such data can be achieved through a series of reloading experiments to obtain isothermal stress-strain data to large strains. However, the lack of a saturation stress as an integral part of the JC and ZA models negates a satisfactory model fit at small strains if these two models were previously optimized for large-strain applications and *vice versa*. Utilization of either the ZA or JC models in large-scale system calculations where portions of the problem simultaneously span from low to high strains, particularly in the case of localization problems, makes optimized fitting of these models nearly impossible. One example of the model-fitting result for unalloyed Ta is shown in Figure 10. The figure shows two curves from the test matrix plotted in Figure 3. Isothermal stress data are calculated to a strain of one to demonstrate the large differences in stress levels at large strains using different approaches for deriving the parameters for all three constitutive models. The ZA model fit previously discussed was optimized to data obtained to a strain of 0.25, as shown in Figure 6. Yield stresses and strain-hardening behavior were described by this best set of parameters extremely well. However, the open circles in Figure 10 at large strains suggest that continual hardening due to the absence of a saturation stress in these models will predict high flow stresses at large strains. The manifestation of this over prediction is that calculations using the finite element method (EPIC code) to simulate the extremely high rate deformation in a ballistic application where the average strain was larger than two showed differences in the final sample shapes. Stiffer mechanical properties were predicted by the JC and ZA models, while the MTS model was closer to the experimental observations.[41] Accordingly, stress-strain data at large strains calculated from the MTS model (open squares in Figure 10) using Eq. [13], along with the experimental data at small strains, were used as inputs to the fitting program to reoptimize the JC and ZA model constants for large-strain behavior. By this method, the physics within the MTS model which incorporates both thermal softening and saturation stress can be utilized to generate high-strain data to serve as input data for fitting the JC and ZA models to large-strain data if not previously measured. The new fit based on the MTS prediction is plotted as the open triangles for the ZA model in Figures 6 and 10. Operationally, there is no significant deviation from the experimental data measured to a strain of 0.25. Detailed examination of the newly fitted curve shown in Figure 6 as

Table IV. Parameters for the MTS Model

Equation	Parameter	Value				Units
		Ta	Ta-2.5W	Ta-5W	Ta-10W	
2	μ_0	65.25	65.25	65.25	65.25	GPa
μ	D	0.38	0.38	0.38	0.38	GPa
	T_0	40	40	40	40	K
10, 14	k/b^3	0.5881	0.5881	0.5881	0.5881	MPa/K
11	σ_a/μ	0.0003	0.0003	0.0003	0.0003	—
σ	$\hat{\sigma}_{i1}/\mu_0$	0.0161	0.0178	0.0171	0.0193	—
	$\hat{\sigma}_{i2}/\mu_0$	0.0053	0.0074	0.0084	0.0124	—
10, 11	g_{0i1}	0.133	0.178	0.210	0.280	—
S_i	g_{0i2}	0.400	0.526	0.585	0.604	—
	g_{normq}	0.157	0.17	0.17	0.17	—
	$\dot{\varepsilon}_{0i}$	10^7	10^7	10^7	10^7	s^{-1}
	q_i	3/2	3/2	3/2	3/2	—
	p_i	1/2	1/2	1/2	1/2	—
10, 11	$\dot{\varepsilon}_{0\varepsilon}$	10^7	10^7	10^7	10^7	s^{-1}
S_ε	$g_{0\varepsilon}$	1.6	1.6	1.6	1.6	—
	q_ε	1	1	1	1	—
	p_ε	2/3	2/3	2/3	2/3	—
13	θ_0	3000	2000	2500	3100	MPa
θ	α	2	1	0.5	0.5	—
14	$g_{0\varepsilon s}$	1.6	1.6	1.6	1.6	—
$\hat{\sigma}_{\varepsilon s}$	$\hat{\sigma}_{\varepsilon s0}$	650	650	750	850	MPa
	$\dot{\varepsilon}_{0\varepsilon s}$	10^7	10^7	10^7	10^7	s^{-1}
15	ρ	16.6	16.6	16.6	16.6	Mg/m^3
ΔT	A_0	0.1455	0.1455	0.1455	0.1455	J/g·K
	A_1	0.09544×10^{-4}	0.09544×10^{-4}	0.09544×10^{-4}	0.09544×10^{-4}	$J/g \cdot K^2$
	A_2	−68.9	−68.9	−68.9	−68.9	$J \cdot K^3/g$
	Ψ	0.95	0.95	0.95	0.95	—

the open triangles for curve number 2 reveals that: (1) yield stress is lower than the experimental value, (2) the stress level is higher than the experimental data at strains less than 0.1, and (3) the stress level is lower than the experimental value at strains above 0.15. Mathematically, unless large-strain data are generated either through nontrivial reloading tests or calculated from an assumed hardening law, there is no unique set of constants to predict large-strain behavior from the small-strain data for the ZA and JC models. The JC and ZA model-fitting parameters so fit which enforce a "saturation" at large strains are listed in Tables II and III with asterisks. The unalloyed Ta data presented in Figure 10 has a different initial hardening behavior, which causes a large difference in these two fitting results, as can be seen by the exponent n in Tables II and III.

In order to demonstrate the differing capabilities for capturing the large-strain behavior by these three constitutive models, pure tantalum in bar form of sufficient size to provide samples to be upset forged to large strains was studied. For the ZA and JC models, the strain-hardening coefficient n depends on the range of strain over which the coefficient was optimized.[42] The best fit to small-strain data of the Ta bar is achieved using $n = 0.575$ for the ZA model. Fixed n values of 0.5, 0.4, and 0.3 were then used to refit the data for high-strain applications *before* the large-strain experimental data was available. The MTS model coefficients were derived based on the same well-controlled low-strain experimental data.

In this study, various plastic strains (0, 0.42, 0.95, and 1.85) in Ta were achieved through upset forging cylinders of the Ta bar at room temperature. Compression samples were subsequently machined from the forged plates to study

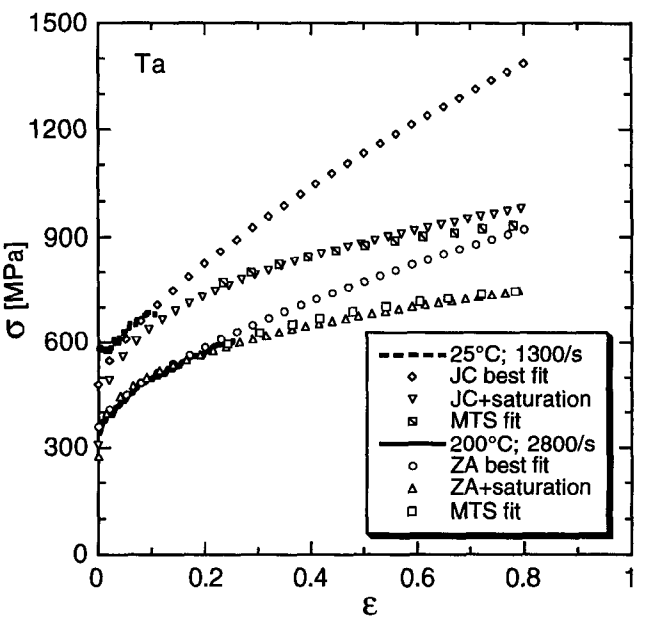

Fig. 10—Experimental data of the tests at 25 °C and 200 °C under high rate compression. The symbols are the results of the model fits for isothermal conditions.

the mechanical properties associated with that degree of prestraining. The thin surface layers, where surface shears due to friction during forging are known to dominate, were machined off the forged plates before the samples were cored from the plates using electrodischarge machining. One needs to keep in mind the effect of deformation history effects on extrapolating large-strain behavior to other load-

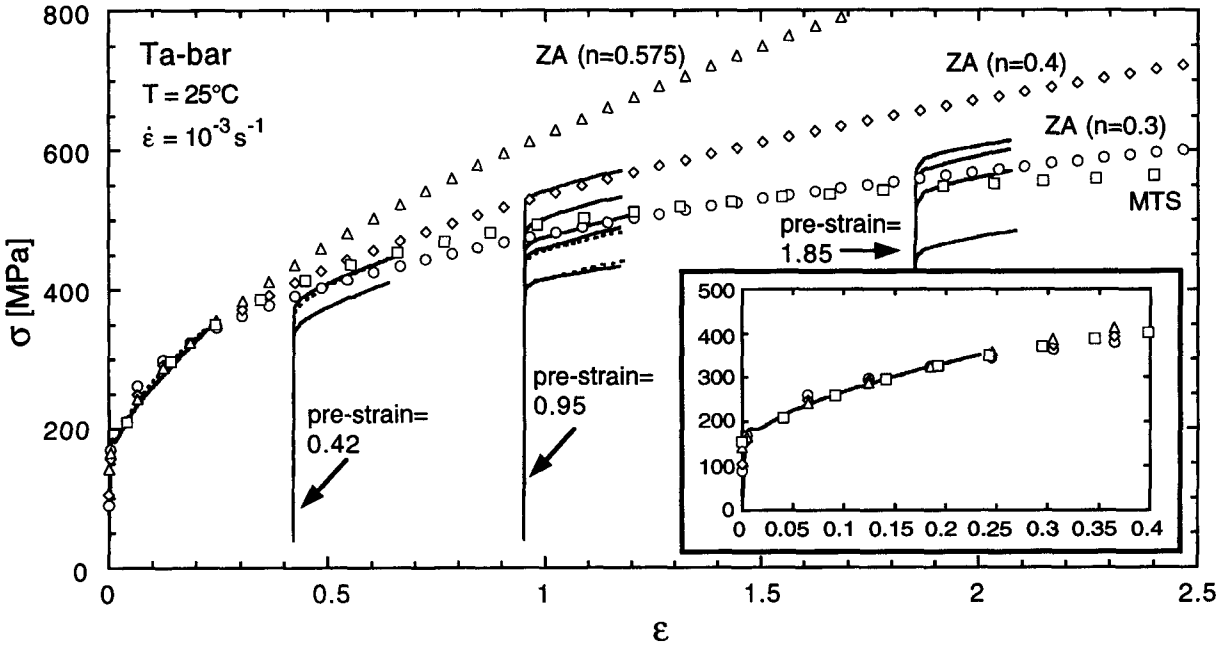

Fig. 11—Compressive stress-strain response of the Ta-bar material as a function of upset forging strain.

ing paths. Tantalum is known to exhibit little or no dependence on deformation path[43] when deformation is dislocation generation and storage dominated. Accordingly, the mechanical property data gathered through reloading the large-strain prestrained plates in this study can, therefore, be used to "check" the fit of the constitutive models to large strains and thereafter applied to other deformation paths.

Prestrained samples were tested in compression at room temperature at a strain rate of 10^{-3} s^{-1}. The reload stress-strain responses after offsetting for the corresponding amount of quasi-static forging prestrain are shown as the solid lines in Figure 11. It is seen that reproducibility in the stress-strain response is diminished after prestraining. The nonhomogeneities in this Ta bar, which were documented elsewhere,[44] clearly identified the existence of banding in the microstructure and a texture gradient in this material. Because of the scatter shown in the stress-strain data, the absolute large-strain behavior is not readily available. Because the reloaded samples were machined from various parts of the upset forged discs, the data can be viewed providing *bounds* on the mechanical response at large strains. Comparison with the model calculations is shown as open symbols in the same figure. The best fit of the ZA model to the small-strain data with $n = 0.575$ leads to an unrealistically high stress level at large strains. Lower n values seem to substantially decrease the stress levels at large strains. For the ZA model, $n = 0.3$ seems to capture the large-strain behavior, even though it totally missed the yield and low-strain flow-stress experimental data (magnified as the insert in this figure). The hardening laws used in the MTS model and in the JC and ZA models are compared in Figure 12. The abscissa in this plot represent the flow stress normalized by the saturation stress, while the ordinate is the strain-hardening rate normalized by the initial strain-hardening rate (θ/θ_0 in Eq. [13]). The solid lines show a few possibilities that phenomenologically describe

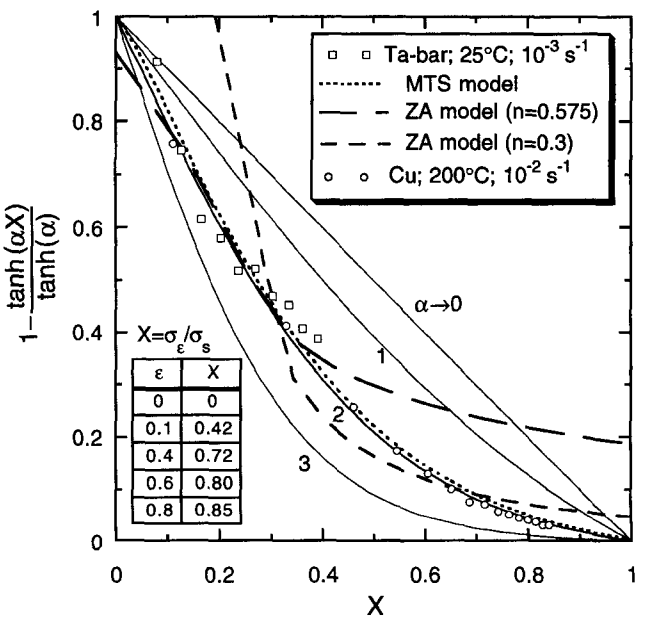

Fig. 12—Hardening curves used in the MTS model (solid lines) plotted with experimental data (symbols). The fit to the ZA model with different hardening exponents (n) to Ta-bar data is shown as the long and medium dashed lines. The insert table is the data of Cu.

the hardening behavior in the MTS model. Experimental data on Cu and the Ta bar are plotted as symbols in this figure. In general, for metallic materials, the strain-hardening rate decreases rapidly after yielding and then slows down at large strains. The flow-stress increment within a fixed strain range at higher strains is smaller than the one accumulated at lower strains. Therefore, the major part of this curve is actually determined by stress-strain data to small strains. In the case of Cu, the normalized stresses *vs* the deformation strains are listed as a table in the figure. At true strain of 0.6, the normalized stress is 0.8, which is

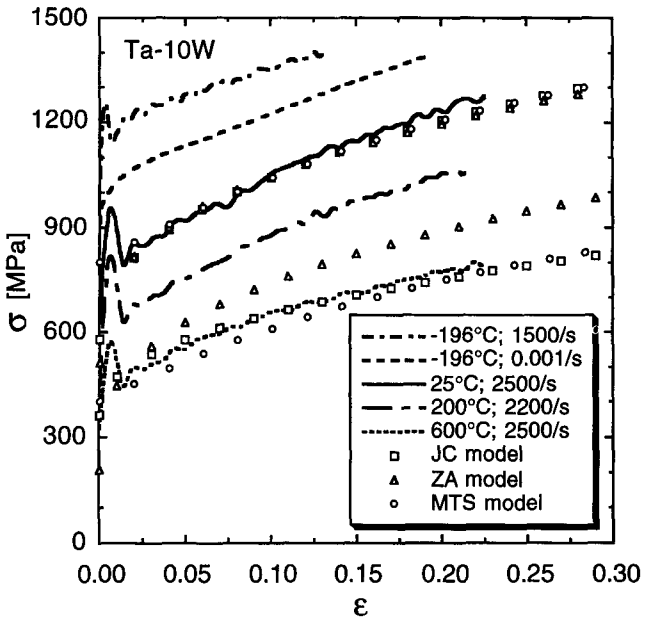

Fig. 13—Stress-strain curves of Ta-10W and a comparison of the JC, ZA, and MTS model fits to the high strain-rate data at 25 °C and 600 °C.

sufficient to determine the hardening parameter α for this material. In the case of Ta bar at 25 °C at 10^{-3} s^{-1}, the hardening curve is represented by the open squares in Figure 12. This hardening curve is well represented by the fit of the hardening part in the MTS model (short dashed line) and the power hardening law in the ZA model with n = 0.575 (long dashed line) to a normalized stress up to 0.4, which is 0.25 in true strain. Reloading this sample to higher strain values (*e.g.*, 0.5) would allow a more accurate description of the hardening curve. However, the reasonably accurate fit to large strains between the calculated data of the MTS model and the experimental data, as has been demonstrated in Figure 11, substantiates the applicability of the hardening law used in the MTS model. The data beyond a normalized stress value of 0.4 in the ZA model show a much higher strain-hardening rate and lead to a high predicted stress level at large strains (open triangles in Figure 11). With a fixed lower n value (= 0.3), the hardening curve (medium dashed line in Figure 12) is close to the one for the MTS model at higher normalized stress, but totally missed the strain-hardening behavior exhibited by the experimental data in the lower normalized stress regime (*i.e.*, small strains). This exercise shows that the hardening behavior in a constitutive model that uses a power-hardening law depends on the strain range within which the coefficients were optimized. The dependence of the n value on the strain range optimized for the ZA and JC models makes it difficult to derive a unique set of material parameters covering a large strain range. The MTS model, due to its inclusion of *approaching* saturation in stress at large strains, is able to satisfactorily *predict* the large-strain behavior based solely upon low-strain data (Figure 11). This comparison in predicting large-strain behavior by different models provides a strong justification for using the hardening law adopted in the MTS model to regenerate the fits to the JC and the ZA models for large-strain applications if either the JC or ZA model has to be used. Furthermore, the "saturation" stress used in the MTS model for this particular strain rate (10^{-3} s^{-1}) and temperature (25 °C) will be achieved when the true strain exceeds a value of seven. This is in excess of the strain range observed in many dynamic loading applications. Therefore, the saturation concept is used as a *limiting condition* for the mechanical response of a material in the MTS model, rather than a *demanding phenomenon* in constructing the model.

Since it is both experimentally difficult and costly to do multiple reloading experiments to achieve large plastic strains at constant high strains at high strain rates, most users[15,45,46] tend to derive, for instance, the strain-hardening exponent n from a single or limited number of low strain-rate stress-strain curves. Based upon studies of a number of cubic materials, it is well known that the hardening behavior at low strain rates is lower than that exhibited in dynamic tests.[35] The MTS model has a strain rate and/or temperature-dependent parameter θ_0 (in Eq. [13]), whose function is to model the hardening behavior of a material as a function of strain rate and/or temperature.

B. *Comparison of Constitutive Modeling Results*

A comparison of the stress-strain and hardening behavior of the unalloyed Ta and Ta-10W for the JC model, the ZA model, and the MTS model is shown in Figure 6, 7, 9, and 13. The ZA model parameters best fit to the unalloyed Ta data over a wide range of temperatures and strain rates as compared to the low-strain experimental data is shown in Figures 6, 7, and 9. The fit to the MTS model can be improved to more accurately capture the yield stresses if some of the parameters in Eq. [16] were allowed to more freely vary within the ranges prescribed. For example, instead of using p_t = 1/2 and q_t = 3/2, which are often suitable, another set of p_t and q_t values can be used. The JC model uses a power-law hardening relation, which is multiplied by the terms representing strain rate and temperature sensitivity (Eq. [3]). Application of this formula to the unalloyed Ta data which exhibits a high rate sensitivity of the flow stress, but an almost rate-insensitive strain-hardening response, shows that calculated stresses deviate substantially from the experimental data. On the other hand, this intrinsically presumed rate and temperature dependence of the yield and flow stress in the JC model as well as the strain-hardening rate quite adequately described the stress-strain behavior of the Ta-10W alloy (Figure 13), in fact better than for the unalloyed Ta (Figure 7).

Our observations have shown that the JC model is more effective for material classes which exhibit moderate strain rate and temperature sensitivity of the yield and flow stresses and the strain-hardening rate, *i.e.*, some fcc alloys. Unfortunately, for most pure metals and many engineering alloys, either the yield and flow stresses are a strong function of temperature and strain rate, and the strain-hardening rate is temperature and strain-rate insensitive (*e.g.*, in Ta and other pure bcc metals), or the yield stress is relatively rate and temperature insensitive but the hardening rate is a strong function of both variables due to a high dynamic recovery rate at large strains (*e.g.*, in Cu and other fcc metals). Overall, the lack of a sufficient physical descriptive basis within the JC model fails to capture the real material properties of a large number of engineering metals except when carefully "tuned" over a very narrow range of experimental conditions, *i.e.*, strains, temperatures, and strain

rates. The stress level at larger strains calculated from using this best set of parameters for the JC and ZA models using power-hardening laws may well be above the actual stress levels obtainable at large strains, as has been shown in Figure 11. Optimizing these model parameters to fit large-strain behavior results in poor model fits to the yield and small-strain data (*e.g.*, fits to 200 °C data as represented by the circles and triangles in Figure 6). The apparent "good" fit of the ZA model to the unalloyed Ta data at small strains is diminished if (1) they are extrapolates to large strains or (2) refit to a different larger strain range. Furthermore, the mandatory strain-hardening rate insensitivity to temperature and strain rate in the ZA model for bcc structures results in unsatisfactory calculations for the stress-strain behavior of the Ta-10W deformed dynamically at 600 °C (Figure 13).

The original ZA model separated the mechanical response of metals into two main classes, namely, those possessing either an fcc or a bcc crystal structure. The constitutive relation for the fcc metals was formulated as

$$\sigma = C_0 + C_2 \cdot \varepsilon_p^n \cdot \exp(-C_3 \cdot T + C_4 \cdot T \cdot \ln \dot{\varepsilon}) \quad [19]$$

This formulation states that yield stress is nominally a constant and that the strain-hardening rate intimately depends on both temperature and strain rate. The degree of rate dependence can vary somewhat depending on alloy content. Neither Eq. [4] nor Eq. [19] can, however, satisfactorily represent the mechanical response of the Ta-10W shown in Figure 13. Nevertheless, the ZA model adequately reproduces most of the pure bcc and fcc metals which fall into the above two distinct categories when accurately "tuned" to a fixed data set.

The MTS model is based on the description of the physical processes and kinetics of dislocations overcoming obstacles. Long-range obstacles such as back stresses can only be overcome due to applied stresses, which are termed athermal barriers, while short-range obstacles, such as impurities, forest dislocations, and Peierls stress can be surpassed by moving dislocations with the assistance of thermally activated processes, in addition to the applied stresses. Each process in the MTS model is described by physically based equations or phenomenologically observed relations. Summation of the contributions from the stresses required to overcome different obstacles yields the flow stress at the current structure for prescribed deformation condition. In the case of yield stress for the unalloyed-Ta and Ta alloys in the current study, the experimental data suggest two different mechanisms are governing the deformation process. With a combination of variables in a physically sound way ($kT \cdot \log(\dot{\varepsilon}_0/\dot{\varepsilon})$), the same form of the constitutive equations can be used with different normalized activation energies (g_{0_ε}) that characterize the corresponding rate-controlling mechanisms. The structure evolution as described by Eqs. [13] and [14] supports the same interpretation. With a large normalized activation energy ($g_{0\varepsilon}$) of 1.6 for unalloyed Ta opposed to 0.312 for copper[14] the dependence of strain hardening on temperature and strain rate as observed in this study on Ta and previous fcc materials is seen to be well represented by the same formulation. This eliminates in the MTS model the need to invoke different empirically observed descriptions, such as the two distinct constitutive equations used for the ZA model for different crystal system materials.* This finding is consistent with the fact that the deformation mechanisms in both bcc and fcc materials are dominated by thermally activated processes under the currently studied deformation conditions.

*Combining Eqs. [4] and [19] into a new constitutive relation was done recently by Zerilli and Armstrong.[47]

VI. CONCLUSIONS

The current study of the influence of tungsten alloying additions on the mechanical properties and constitutive modeling of tantalum indicates the following.

1. Tungsten alloying additions significantly increase the yield and flow-stress levels attained and also increase the rate of work hardening in Ta-W alloys compared to unalloyed tantalum, under both quasi-static and dynamic strain rates.
2. The high strain-rate and temperature sensitivity of the flow stress and the insensitivity of the strain-hardening rate indicate that the rate-controlling mechanism for deformation at high strain rate from low to intermediate temperatures in Ta and Ta-W alloys is thermal activation over the Peierls stress. At higher temperatures, the yield stresses become less rate and temperature dependent indicating a change in the rate-controlling mechanism. Alloying with W makes this change less apparent due to an increase in the importance of dislocation-solute interactions when the solute concentration is increased. Overall, the temperature and strain-rate sensitivities are changed upon alloying tantalum with tungsten.
3. Three constitutive relations, namely, the JC, ZA, and MTS models, have been examined to describe the stress-strain rate-temperature relations of Ta and Ta-W alloys in the high strain-rate regime. It is shown that the empirical relations used in the JC and ZA models for strain hardening ($\sigma_0 + K \cdot \varepsilon^n$) may introduce substantial deviations from the actual stress levels at large strains. The physically based MTS model is demonstrated to overall provide better fitting results to the Ta and Ta-W alloys investigated. The stresses at large strains calculated using the MTS model can be used to regenerate the parameters for the JC and ZA models for high strain applications when only experimental data at low strains are readily available.

ACKNOWLEDGMENTS

This work was supported under the auspices of the United States Department of Energy. The authors acknowledge the assistance of M.F. Lopez and R.W. Carpenter, Jr., for conducting the mechanical tests. The authors acknowledge Cabot Corporation for providing some of the tantalum materials studied.

REFERENCES

1. W. Kock and P. Paschen: *J. Met.*, 1989, vol. 41, pp. 33-39.
2. R.J. Arsenault and A. Lawley: *Work Hardening*, J.P. Hirth and J. Weertman, eds., Gordon and Breach, New York, NY, 1968, pp. 283-309.

3. G.T. Gray III and A.D. Rollett: *High Strain Rate Behavior of Refractory Metals and Alloys*, R. Asfhani, E. Chen, and A. Crowson, eds., TMS, Warrendale, PA, 1992, pp. 303-15.
4. J.B. Clark, R.K. Garrett, Jr., T.L. Jungling, and R.I. Asfahani: *Metall. Trans. A*, 1991, vol. 22A, pp. 2959-68.
5. J.B. Clark, R.K. Garrett, Jr., T.L. Jungling, and R.I. Asfahani: *Metall. Trans. A*, 1992, vol. 23A, pp. 2183-91.
6. A. Gilbert, D. Hull, W.S. Owen, and C.N. Reid: *J. Less-Common Met.*, 1962, vol. 4, pp. 399-408.
7. J.W. Christian: *Metall. Trans. A*, 1983, vol. 14A, pp. 1237-56.
8. W.H. Gourdin, D.H. Lassila, M.M. LeBlanc, and A.L. Shields: *J. Phys. IV*, 1994, pp. C8-207-C8-212.
9. K.G. Hoge and A.K. Mukherjee: *J Mater. Sci.*, 1977, vol. 12, pp. 1666-72.
10. R.A. Foxall and C D. Statham: *Acta Metall.*, 1970, vol. 18, pp. 1147-58.
11. P.J. Maudlin, R.F. Davidson, and R.J. Henninger: Report No. LA-11895-MS, Los Alamos National Laboratory, Los Alamos, NM, 1990.
12. M.N. Raftenberg: Report No. BRL-TR-3363, United States Army Ballistic Research Laboratory, Maryland, 1992.
13. A.M. Rajendran and P. Woolsey: Report No. ARL-TR-216, United States Army Research Laboratory, Maryland, 1993.
14. P.S. Follansbee and U.F. Kocks: *Acta Metall.*, 1988, vol. 36, pp 81-93.
15. G.R. Johnson and W.H. Cook: *Proc. 7th Int. Symp. on Ballistic*, The Hague, The Netherlands, 1983, pp. 541-47.
16. F.J. Zerilli and R.W. Armstrong: *J. Appl. Phys.*, 1987, vol. 61, pp. 1816-25.
17. G.R. Johnson and Stryk. Report No. AFATL-TR-86-51, Air Force Armament Laboratory, Eglin Air Force Base, Florida, 1986.
18. D.J. Caliostro, D.A Mandell, and L.A. Schwalbe: *Int J. Impact Eng.*, 1990, vol. 10, pp. 81-92.
19. J.O. Hallquist: Report No. UCID-19592, Rev. 4, Lawrence Livermore National Laboratory, Livermore, CA, 1988.
20. G.T. Gray III, S.R. Bingert, S.I. Wright, and S.R. Chen: *High Temperature Silicides and Refractory Alloys*, C.L. Briant, J.J. Petrovic, B.P. Bewlay, A.K. Vasudevan, and H.A. Lipsitt, eds., Materials Research Society, Pittsburgh, PA, 1994, vol. 322, pp. 407-12.
21. P.S. Follansbee: *High Strain Rate Compression Testing—The Hopkinson Bar*, 9th ed., ASM, Metals Park, OH, 1985, vol. 8, pp. 198-203.
22. G. Simmons and H. Wang: *Single Crystal Elastic Constants and Calculated Aggregate Properties: A Handbook*, 2nd ed., The MIT Press, Boston, MA, 1991.
23. Y.P. Varshni. *Phys. Rev. B*, 1970, vol. 2, pp. 3952-58.
24. S.R. Chen and G.T. Gray III: *2nd Int. Conf. on Tungsten and Refractory Metals*, A. Bose and R.J Dowding, eds., Oct. 17–19, McLean, VA, Metal Powder Industries Federation, Princeton, NJ, 1995, pp. 489-98.
25. P.S. Follansbee and G.T. Gray III: *Metall. Trans. A*, 1989, vol. 20A, pp. 863-74.
26. P.S. Follansbee, J.C. Huang, and G.T. Gray III: *Acta Metall.*, 1990, vol. 38, pp. 1241-54.
27. U.F. Kocks, A.S. Argon, and M.F. Ashby: *Thermodynamics and Kinetics of Slip*, Progress in Materials Science, Pergamon Press, New York, NY, 1975, vol. 19.
28. U.F. Kocks: *J. Eng. Mater. Technol., Trans. ASME*, 1976, vol. 98, pp. 76-85.
29. P. Hassen: *Phil. Mag.*, 1958, vol. 3, pp. 384-418.
30. G. Schoeck and A. Seeger: *Defects in Crystalline Solids*, Physical Society, London, 1955.
31. B.L. Mordike, K.D. Rogausch, and A.A. Braithwaite: *Met Sci. J.*, 1970, vol. 4, pp. 37-40.
32. F.J. Zerilli and R.W. Armstrong: *J. Appl. Phys.*, 1990, vol. 68, pp. 1580-91.
33. *Thermodynamic Properties of the Elements*, D.R. Stull and G.C. Sinke, eds., American Chemical Society, Washington, DC, 1956.
34. S.R. Chen and G T. Gray III: to be submitted.
35. G.T. Gray III, S.R. Chen, W. Wright, and M.F. Lopez: Report No. LA-12669-MS, Los Alamos National Laboratory, Los Alamos, NM, 1994.
36. H. Conrad: *J. Met*, 1964, vol. 16, pp. 582-88.
37. A.H. Cottrell: *Dislocation and Plastic Flow in Crystals*, Clarendon Press, Oxford, United Kingdom, 1953.
38. P Ludwik: *Elemente der Technologischen Mechanik*, Springer, Berlin, 1909.
39. D.A. Hughes and W.D. Nix: *Metall Trans. A*, 1988, vol. 19A, pp. 3013-24.
40. A.D. Rollett. Ph.D. Thesis, Drexel University, Philadelphia, PA, 1988.
41. P.J. Maudlin: Report No. LA-12960-PR: The Joint DoD/DOE Munitions Technology Development Program Progress Report for 1994—"Unconventionally Processed High-Density Materials," Los Alamos National Laboratory, Los Alamos, NM, 1995.
42. G.T. Gray III, S.R. Chen, and K.S. Vecchio: 1996, to be submitted.
43. G.T. Gray III and K.S. Vecchio: *Metall. Trans A*, 1995, vol. 26A, pp. 2555-62.
44. G.T. Gray III, S.R. Chen, S.R. Bingert, S.I. Wright, and P.J. Maudlin: The Joint DoD/DOE Munitions Technology Development Program, Los Alamos National Laboratory, Los Alamos, NM, 1996.
45. T.J. Holmquist and G.R Johnson: *J Phys. IV*, 1991, pp. C3-853-C3-860.
46. C.L. Wittman and C.M. Lopatin: *Tungsten & Tungsten Alloys—1992*, A. Bose and R.J. Dowding, eds., Metal Powder Industries Federation, Princeton, NJ, 1992, pp. 357-64.
47. F.J. Zerilli and R.W. Armstrong: *Symp. on High Strain Rate Effects*, San Francisco, CA, 1995.